PCCP

PAPER

Internal structure, hygroscopic and reactive properties of mixed sodium methanesulfonate-sodium chloride particles

Y. Liu,[†][a] B. Minofar,[‡][b] Y. Desyaterik,[§][a] E. Dames,[c] Z. Zhu,[a] J. P. Cain,[c]
R. J. Hopkins,[¶][d] M. K. Gilles,[d] H. Wang,[c] P. Jungwirth[e] and A. Laskin*[a]

Internal structures, hygroscopic properties and heterogeneous reactivity of mixed CH_3SO_3Na/ $NaCl$ particles were investigated using a combination of computer modeling and experimental approaches. Surfactant properties of $CH_3SO_3^-$ ions and their surface accumulation in wet, deliquesced particles were assessed using molecular dynamics (MD) simulations and surface tension measurements. Internal structures of dry $CH_3SO_3Na/NaCl$ particles were investigated using scanning electron microscopy (SEM) assisted with X-ray microanalysis mapping, and time-of-flight secondary ion mass spectrometry (TOF-SIMS). The combination of these techniques shows that dry $CH_3SO_3Na/NaCl$ particles are composed of a NaCl core surrounded by a CH_3SO_3Na shell. Hygroscopic growth, deliquescence and efflorescence phase transitions of mixed $CH_3SO_3Na/NaCl$ particles were determined and compared to those of pure NaCl particles. These results indicate that particles undergo a two step deliquescence transition: first at ~69% relative humidity (RH) the CH_3SO_3Na shell takes up water, and then at ~75% RH the NaCl core deliquesces. Reactive uptake coefficients for the particle–HNO_3 heterogeneous reaction were determined at different $CH_3SO_3Na/NaCl$ mixing ratios and RH. The net reaction probability decreased notably with increasing CH_3SO_3Na and at lower RH.

Introduction

Over the last few decades, the fundamental kinetics and mechanisms of heterogeneous reactions on atmospheric particles have been of interest due to their impact on the

[a] *William R. Wiley Environmental Molecular Sciences Laboratory, Pacific Northwest National Laboratory, P. O. Box 999, MSIN K8-88, Richland, WA 99352, USA. E-mail: Alexander.Laskin@pnl.gov; Fax: (509) 376-6139; Tel: (509) 371-6129*
[b] *Institute of Systems Biology and Ecology of the Academy of Sciences of the Czech Republic and Institute of Physical Biology, University of South Bohemia Zamek 136, Nove Hrady, Czech Republic*
[c] *Department of Aerospace and Mechanical Engineering, University of Southern California, Los Angeles, CA 90089-1453, USA*
[d] *Chemical Sciences Division, Lawrence Berkeley National Laboratory, Berkeley, CA 94720, USA*
[e] *Institute of Organic Chemistry and Biochemistry, Academy of Sciences of the Czech Republic, and Center for Complex Molecular systems sand Biomolecules, Flemingovo nam. 2, Prague 6, CZ-16610, Czech Republic*
† Present address: Department of Chemistry, University of Colorado, Denver, CO 80217, USA.
‡ Present address: Department of Chemistry, Faculty of Science, Kyushu University, Hakozaki, Higashi-ku, Fukuoka city, 6-10-1,812-8581, Japan.
§ Present address: Department of Atmospheric Science, Colorado State University, Fort Collins, CO 80523, USA.
¶ Present address: Detection Department, The Defence Science and Technology Laboratory, Porton Down, Salisbury, Wiltshire, SP4 0JQ, U.K.

atmospheric environment and climate change. Sea salt aerosol, generated by wave action and bubble bursting at the ocean surface, have the second largest global burden by mass.[1] Airborne sea salt particles undergo heterogeneous reactions with trace atmospheric species, including OH, HNO_3, O_3, NO_2, N_2O_5 and $ClONO_2$. In some of these reactions, photo-chemically inert halides present in sea salt can be converted to reactive halogen species $X^\bullet$ and $XO^\bullet$ (X = Cl and Br). These halogen species can impact the ozone budget and oxidative capacity of the atmosphere.[2]

A noticeable halide deficit in sea salt aerosols is reported in a number of field studies at various geographic locations.[3–9] In regions where sea salt particles are impacted by anthropogenic pollutants, the reaction of gas-phase nitric acid with sodium chloride

$$NaCl(s,aq) + HNO_3(g) \rightarrow NaNO_3(aq) + HCl(g) \quad (R1)$$
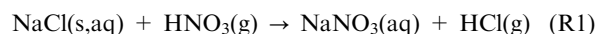
is regarded as a major contributor to halide depletion and nitrate enrichment.[10–24] Reaction 1 is also a net sink of atmospheric nitric acid, and hence regulates the gas-particle partitioning of HNO_3 and consequently impacts the atmospheric and aquatic environments.[2,25]

Similarly, sea salt particles also react with biogenic sulfur-containing acids through corresponding aqueous chemistry in deliquesced particles. Dimethyl sulfide (CH_3SCH_3, DMS) produced by marine phytoplankton is the largest source of

sulfur containing species over the ocean.[26] DMS undergoes oxidation through a complex series of reactions with gas and liquid phase oxidants through two main pathways: hydrogen abstraction and oxygen addition.[27,28] The H-abstraction channel yields sulfur dioxide (SO_2) which ultimately forms sulfuric acid (H_2SO_4), whereas the oxygen addition produces methane-sulfonic acid (CH_3SO_3N, MSA) and a number of intermediate products, such as dimethylsulfoxide (CH_3SOCH_3, DMSO), dimethylsulfone ($CH_3SO_2CH_3$, DMSO_2), and methanesulfonic acid ($CH_3S(O)OH$, MSIA).[27,28] Computer models of the multi-phase marine boundary layer (MBL) chemistry show that H_2SO_4 is the only product that can nucleate new particles.[28] All other products condense onto preexisting sea salt particles where they can also contribute to chloride depletion. Consequently, the HCl acid displacement reaction of sea salt particles can be expressed more generally as:

$$Na^*Cl \ (s,aq) + HA(g,aq) \rightarrow Na^*A \ (aq) + HCl \ (g,aq)$$
(R2)
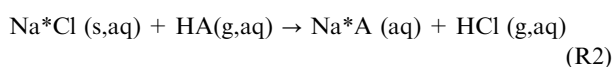
where HA denotes acids, such as HNO_3, H_2SO_4, SO_2/H_2O, MSA, MSIA, and Na* depicts Na^+ as well as a variety of other cations present in sea salt, e.g., Mg^{2+}, K^+, Ca^{2+}. Table 1 shows the standard Gibbs free energies of selected aqueous reactions involving H_2SO_4, CH_3SO_3N, and HNO_3. Thermodynamics favor R2 for a wide range of acids. These acid displacement reactions are driven by the release of volatile HCl and reportedly account for the formation of nitrate, non-sea-salt-sulfate (nss-SO_4^{2-}) and methanesulfonate in aged sea salt particles.[5,7–9,16,29,30] However, subsequent reactions of CH_3SO_3Na and Na_2SO_4 salts with HNO_3 are not thermo-dynamically favored. This implies that formation of sulfates and methanesulfonates in sea salt particles reduces their capacity to act as a sink for HNO_3. Additionally, formation of methanesulfonate in sea salt particles is thermodynamically favored over sulfate formation.

Sea salt particles are naturally multicomponent because of the original complex composition of sea water. Their chemical composition is further complicated by interactions with biogenic and anthropogenic oxidants. These processes lead to composition and concentration changes in sea salt aerosol, and ultimately affect its chemical reactivity and physical properties. For many years, the DMS $\rightarrow$ SO_2 $\rightarrow$ H_2SO_4 reaction sequence was assumed to be the dominant reaction pathway for DMS oxidation in the MBL, and significant attention was given to the physico-chemical properties of the mixed sea salt/sulfate particles.[31–34] However, recent modeling[28] and field studies[30] indicate that under certain conditions the DMS $\rightarrow$ CH_3SO_3H

oxidation pathway contributes substantially and yields elevated concentrations of $CH_3SO_3^-$ in sea salt particles. For instance, our recent field study reported characteristic $CH_3SO_3^-$/nss-SO_4^{2-} ratios of 0.6 and the total-S/Na ratio of 0.15 in sea salt particles collected in the area of cold ocean current along the northern California coast.[30] Yet, the chemistry and properties of mixed sea salt/methanesulfonate particles have not been well characterized.

Because of rapid aqueous-phase diffusion, most ionic species in liquid (deliquesced) sea salt particles are distributed homogeneously. Nevertheless, surface enhancement or depletion in mixed droplets could occur due to the difference in ion polarizability and lyophobic nature of some species. Unlike nitrate and sulfate ions, methanesulfonate ions are surfactants,[35,36] and accumulate on the surface of deliquesced particles. Since methalsulfonate salts are more soluble than NaCl, the surface accumulation of $CH_3SO_3^-$ can be enhanced upon dehydration at decreasing RH.

In this work, we investigate the structure and physical properties of mixed $CH_3SO_3Na/NaCl$ particles and the resulting effects of CH_3SO_3Na on the hygroscopic properties and chemical reactivity of NaCl particles, which we use as a laboratory proxy for mixed methanesulfonate/sea salt particles. First, we present results of molecular dynamics (MD) simulations and surface tension measurements to infer the internal distribution of ionic species within liquid (deliquesced) particles. Second, we present experimental observations of the morphological/chemical structure of dried particles using methods of microscopic chemical imaging and depth profiling that confirmed shell-core structure of mixed $CH_3SO_3Na/NaCl$ particles. Finally, we discuss the observed shell-core structure of particles in the context of the hygroscopic properties and humidity-specific kinetics of their heterogeneous reaction with HNO_3.

Computational and experimental methods

Molecular dynamics calculations

Classical molecular dynamics (MD) simulations of CH_3SO_3Na in water and in concentrated aqueous solutions of NaCl and Na_2SO_4 were performed in the standard aqueous slab geometry[37] with the interfaces perpendicular to the z-axis of the simulation box. A tetragonal prismatic unit cell was used with dimensions of 30 Å $\times$ 30 Å $\times$ 100 Å which contained 864 water molecules. All systems included 10 $CH_3SO_3^-$ and Na^+ ions (corresponding to ~0.8 M). In the simulated concentrated solutions, additional 96 Na^+ and Cl^-, or 192 Na^+ and

Table 1 Standard Gibbs free energy of reactions[a]

	Reaction	ΔG_r^o (kJ/mol)
i	$NaCl_{(aq)} + H_2SO_{4(aq)} \rightarrow NaHSO_{4(aq)} + HCl_{(aq)}$	-11.4
ii	$2NaCl_{(aq)} + H_2SO_{4(aq)} \rightarrow Na_2SO_{4(aq)} + 2HCl_{(aq)}$	-0.1
ii	$NaCl_{(aq)} + CH_3SO_3H_{(aq)} \rightarrow CH_3SO_3Na_{(aq)} + HCl_{(aq)}$	> -15.8
iv	$NaCl_{(aq)} + HNO_{3(aq)} \rightarrow NaNO_{3(aq)} + HCl_{(aq)}$	0
v	$Na_2SO_{4(aq)} + 2HNO_{3(aq)} \rightarrow 2NaNO_{3(aq)} + H_2SO_{4(aq)}$	0.1
vi	$CH_3SO_3Na_{(aq)} + HNO_{3(aq)} \rightarrow NaNO_{3(aq)} + CH_3SO_3H_{(aq)}$	6.8
vii	$Na_2SO_{4(aq)} + 2CH_3SO_3H_{(aq)} \rightarrow 2CH_3SO_3Na_{(aq)} + H_2SO_{4(aq)}$	> -22.5

[a] See Appendix A for values of the Gibbs free energy of formation.

96 SO_4^{2-} (∼6 M) ions were added. By applying periodic boundary conditions at a constant volume, an infinite slab with two water/vapor interfaces perpendicular to the z-axis was produced.[38]

In all MD simulations the non-bonded interactions were terminated at 12 Å and long-range electrostatic interactions were accounted for using the particle mesh Ewald procedure.[39] The energy of each of the systems was first minimized (10 000 steps of steepest descent minimization) to avoid bad contacts. Then the systems were equilibrated for several hundred pico-seconds before a 2 ns simulation run. Simulations were performed at 300 K with 1 fs time steps. Hydrogen bonds were constrained using the SHAKE algorithm.[40] Geometries and energy data were recorded every 500 steps. A polarizable force field was employed in all simulations. For water, the POL3 model[41] was used. Potential parameters for $CH_3SO_3^-$ were constructed using the general amber force field (GAFF) set,[42] while those of other ions were taken from a previous study.[43] Fractional charges for the anions were evaluated using the standard RESP procedure employing the Gaussian 03 package.[44] The partial charges, Lennard-Jones parameters, and polarizabilities of all ions are presented in Table 2. All polarizable molecular dynamics (MD) simulations were performed using the Amber 8 program package.[45]

Surface tension measurements

The Wilhelmy plate method[46–48] was used to measure equilibrium surface tension of aqueous solutions. Prior to the experiments, a platinum Wilhelmy plate was dipped into a 50 : 50 (v/v) mixture of nitric and sulfuric acids, washed in deionized water, and heated overnight at 200 °C. The plate was attached to a microbalance via a thin metal wire and placed over the bottom of a beaker. An aqueous solution of known concentration was added to the beaker dropwise until the lower edge of the platinum plate was immersed into the water layer. The force on the plate due to wetting was measured by the microbalance and used to calculate surface tension according to the Wilhelmy equation.[46] Measurements were carried out for aqueous solutions of NaCl, Na_2SO_4, $NaNO_3$, CH_3SO_3Na and CH_3SOCH_3 over the concentration range of 0.5 to 4 M for each solute.

Preparation of particle samples for chemical imaging, hygroscopic, and kinetics studies

Nearly monodisperse, mixed CH_3SO_3Na/NaCl particles were prepared by atomizing an aqueous 0.5 M solution of NaCl and CH_3SO_3Na (both from Aldrich, Inc., 99.99% purity) with the CH_3SO_3Na-to-NaCl molar mixing ratio ranging from 0.01 to 0.1.

Table 2 Parameters of the Lennard-Jones potential (σ and ε), polarizabilities (α) and partial electric charges used in MD calculations

Ions	Atoms	σ (Å)	ε (eV)	α	Partial electric charge
$CH_3SO_3^-$	C	1.9080	0.1094	0.878	−0.260
	H	1.4870	0.0157	0.135	0.012
	S	2.0000	0.2500	2.900	1.32
	O	1.6612	0.2100	0.434	−0.70
SO_4^{2-}	S	1.9924	0.2500	0.0	2
	O	1.7680	0.2	1.4	−1
Cl^-	Cl	2.4350	0.100	3.69	−1
Na^+	Na	1.319	0.130	0.24	1

Prior to sizing and deposition, the particles were dried in a diffusion drier (TSI, Inc., Model 3062). Dry particles were deposited onto TEM grid substrates (Carbon Type-B, 400 mesh nickel grids, Ted Pella, Inc.) and silicon wafer chips mounted on the impaction plate of the 5th stage of a micro-orifice uniform deposit impactor (MOUDI) (MSP, Inc., Model 110). The aerodynamic cutoff size of the fifth stage is 1.0 μm. As in previous studies,[49–52] the size uniformity of deposited particles was confirmed by computer-controlled scanning electron microscopy (CCSEM) analysis over 2000 particles on several different grids. The number size distributions of deposited CH_3SO_3Na/NaCl particles were log-normal with median diameters approximately of 0.85 μm ($\bar{D}p$), measured as equivalent circle diameters of projected areas of particles in microscopy images.

Particle analyses

Computer-controlled scanning electron microscopy with energy dispersed analysis of X-rays (CCSEM/EDX) was used to determine the elemental composition and loading density of substrate-deposited particles. The microscope is equipped with an EDAX spectrometer (EDAX, Inc., Model PV7761/54 ME) that has an Si(Li) detector 30 mm^2 in active area and an ATW2 window. The system is equipped with Genesis™ hardware and software (EDAX, Inc.) for computer-controlled analyses. The X-ray spectra were acquired for a period of 10 s under a beam current of ∼500 pA and an accelerating voltage of 20 kV. For quantification of the EDX results, the Genesis™ software utilizes a microanalysis method that relates X-ray intensities to elemental concentrations through theoretically calculated equivalent intensities of corresponding peaks.[53] Details of the CCSEM/EDX particle analysis can be found elsewhere.[54]

A TRIFT II time-of-flight secondary ion mass spectrometer (TOF-SIMS) (Physical Electronics, Inc.) was used for imaging and depth profiling of dry CH_3SO_3Na/NaCl particles. The particles collected on silicon wafer chips were placed in a sample holder and subject to a $^{69}Ga^+$ source of primary ions in high-spatial resolution mode. An accelerating voltage of 25 kV and a $^{69}Ga^+$ dose rate of 5.6×10^{17} ions cm^{-2} were used. A combination of static and dynamic modes of operation allowed depth-profiled speciation of different ions characteristic of individual particles.[52,55]

Hygroscopic growth experiments

Hygroscopic properties of CH_3SO_3Na/NaCl particles were studied using a micro-FT-IR spectrometer. Detailed descriptions of the micro-FTIR experimental apparatus, the sample cell, and relevant experimental procedures are reported elsewhere.[51,52] Briefly, the apparatus comprises a Bruker A590 IR microscope equipped with a liquid nitrogen cooled Mercury-Cadmium-Telluride (MCT) detector and interfaced with a FTIR spectro-meter (Bruker, Model IFS 66/S). TEM grids containing particle samples are placed in a temperature-controlled sealed environmental stage (Linkam™, Model THMS 600). The RH over the substrate is controlled by a nitrogen flow at ∼1 L min^{-1} with a controlled humidity from a dew point generator (LI-COR™, Model LI-610). A dew point hygrometer (Vaisala™, Model HMP234) measured the RH. Hygroscopic

growth measurements were carried out at room temperature of $T = 23\ ^\circ\text{C}$. Spectra were acquired by co-adding 512 scans at a resolution of 4 cm^{-1}. The total scan time was 3.2 min. Condensed-phase water was confirmed by the OH stretching and bending modes at ~ 3400 and ~ 1640 cm^{-1}, respectively. The integrated absorbance between 3660 to 2750 cm^{-1} (OH stretch) was used to determine deliquescence relative humidity (DRH) and efflorescence relative humidity (ERH).

Kinetic measurements of HNO$_3$ heterogeneous uptake on particles

Kinetic uptake coefficient of HNO$_3$(g) on mixed CH$_3$SO$_3$Na/NaCl particles was determined using the Particle-on-Substrate Stagnation Flow Reactor (PSSFR) technique described elsewhere.[49] In each experiment a single TEM grid loaded with CH$_3$SO$_3$Na/NaCl particles of a known number density per sample area (N_s) was exposed to a constant flow of nitrogen doped with HNO$_3$ and H$_2$O with known mixing ratios. Flow rate of a HNO$_3$/H$_2$O/N$_2$ mixture was controlled by mass flow controllers. The reactor was passivated prior to each experiment for a minimum of 2 h with a flow of the HNO$_3$/H$_2$O/N$_2$ mixture to ensure no significant loss of HNO$_3$ on the walls of the apparatus and its gas lines. Particles were first wetted by a flow of moist air (RH = 80%) generated by a dew point generator (Li-Cor, Inc., Model LI-610) for 2 min prior to switching on a gas stream of the HNO$_3$/H$_2$O/N$_2$ mixture with selected RH and HNO$_3$ concentration. During each experiment, both RH and HNO$_3$ concentration were monitored continuously by an inline RH sensor (Honeywell, inc., model HIH4000) and a chemiluminescence NO$_y$ analyzer (Thermo Environmental, Inc., model 42C-Y), respectively. The fluctuations were less than 1% and 5% in RH and HNO$_3$ concentration, respectively.

The experimental protocol is similar to that used in previous studies.[49,56] CCSEM/EDX analysis was used to measure the overall Cl$^-$ loss from the reacted CH$_3$SO$_3$Na/NaCl particles, which can be expressed as follows:

$$-\frac{\text{d}[\text{Cl}^-]_d}{\text{d}t} = k_I[\text{Cl}^-]_d \qquad (1)$$

where brackets denote molar concentration, the subscript d denotes the NaCl droplet and t is the reaction time. The apparent, pseudo first-order rate constant k_I is nearly time invariant over the range of reaction time studied, as shown in the previous NaCl and CaCO$_3$ studies,[50,57] and its value may be determined from

$$k_I = -\frac{1}{t}\ln\left(\frac{[\text{Cl}^-]_{d,t}}{[\text{Cl}^-]_{d,t=0}}\right) = -\frac{1}{t}\ln\left(\frac{[\text{Cl/Na}]_t^{\text{EDX}}}{[\text{Cl/Na}]_{t=0}^{\text{EDX}}}\right) \qquad (2)$$

whereas Cl/Na ratios are measured in individual particles by the CCSEM/EDX analysis. For the approach employed here, a formal stoichiometry of reaction R1 is assumed and changes in [Cl$^-$] are used for rate constant calculations. Previous results[57] demonstrated that the reaction stoichiometry is conserved under these experimental conditions. As will be shown in this work, CH$_3$SO$_3$Na is nearly inert to HNO$_3$. Hence, the presence of a small amount of CH$_3$SO$_3$Na is not expected to affect the stoichiometry of R1. In principle,

enrichments of O and N could be also used for determining k_I, but quantitative detection of these low-Z elements is not as accurate as Cl detection because of inherent constraints of the CCEM/EDX analysis.[54]

The uptake coefficient was determined from measurements of the pseudo first-order rate constant k_I, as will be discussed below. The effect of CH$_3$SO$_3$Na on the reactive uptake HNO$_3$(g) on NaCl particles was examined in detail. The uptake coefficients were determined for deliquesced CH$_3$SO$_3$Na/NaCl particles at 80% RH for two CH$_3$SO$_3$Na/NaCl mixing ratios (0.05 and 0.1), and a range of particle loadings ($N_s = 5 \times 10^4$ to 7×10^6 cm^{-2}). The limit of low particle loading ($N_s < 10^5$ cm^{-2}) where the uptake coefficient represents that of a single particle was determined in these experiments, following the procedure established in a previous study.[56] In the second series of experiments, RH = 40% was selected, and CH$_3$SO$_3$Na/NaCl mixing ratios were varied from 0.01 to 0.1. To ensure that the uptake coefficient represents that of a single particle, the experiments were performed with a subset of samples with the particle density below 10^5 cm^{-2}. Experiments were also carried out at 20 and 60% RH to further investigate the humidity effect on the HNO$_3$ uptake.

For the vast majority of measurements, free stream HNO$_3$ concentrations ranged from 4 to 13.5 ppb, similar to the 10–20 ppb level in polluted environments.[58] High HNO$_3$ concentrations (~ 80 ppb) were used only to probe the reactivity of pure CH$_3$SO$_3$Na with HNO$_3$. Most samples had less than 30% chloride depletion upon exposure to HNO$_3$.

Results and discussion

Internal composition of deliquesced and Dry CH$_3$SO$_3$Na/NaCl particles

MD simulations and measurements of surface tension over bulk solutions were used to infer the internal distribution of ionic species in deliquesced CH$_3$SO$_3$Na/NaCl particles. Pure NaCl particles at 75% RH have an approximate water-to-solute ratio (WSR) of 9,[52,59,60] which corresponds to approximately 6 M concentration. To match this ratio, MD modeling included 864 water molecules, 96 NaCl molecules and 10 CH$_3$SO$_3$Na molecules simulated in slab geometry. Additional simulations were performed for 864 H$_2$O, 96 Na$_2$SO$_4$ and 10 CH$_3$SO$_3$Na molecules to explore the effects of sulfates on the surface partitioning of methanesulfonate. The distribution of species at the air–water interface was quantified using density profiles, $i.e.$, averaged abundances of ions and water molecules across the simulated slab. Fig. 1 shows density profiles of the species present in an ~ 0.8 M CH$_3$SO$_3$Na aqueous solution with ~ 6 M of NaCl (panel a) and ~ 6 M of Na$_2$SO$_4$ (panel b) normalized such that the integrals under all the curves are identical. A strong surface propensity of CH$_3$SO$_3^-$ is observed in both cases, exemplified by large surface peaks of its C and S atoms. These two density profiles also reveal that this anion prefers an orientation at the surface with the SO$_3^-$ group oriented toward the aqueous bulk, and the methyl group pointed into the vapor. This particular orientation is graphically illustrated by a snapshot of the CH$_3$SO$_3$Na/Na$_2$SO$_4$/water slab, as shown in Fig. 2 where the
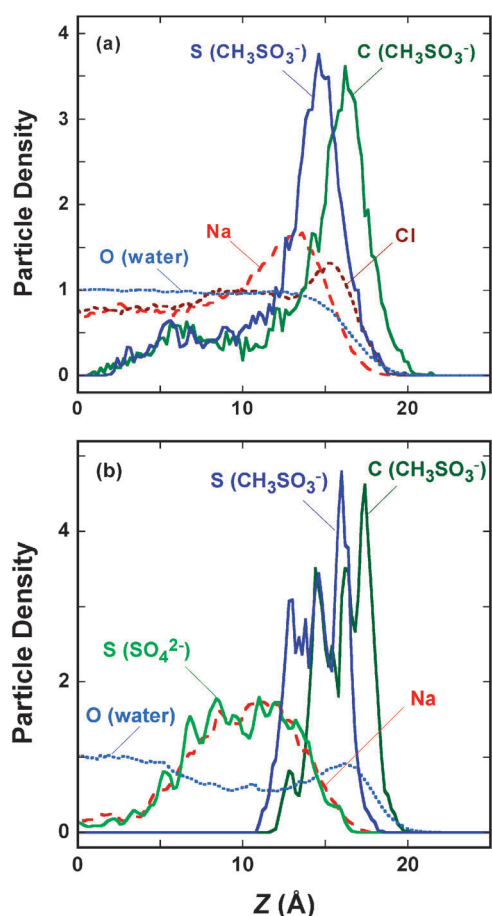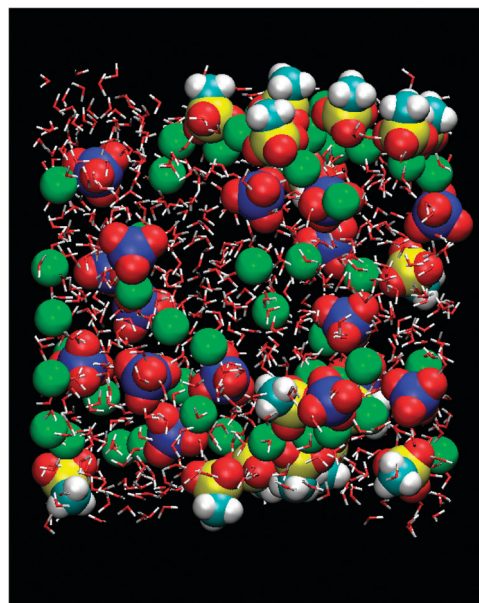
Fig. 1 Density profiles (arbitrary units) from two molecular dynamics (MD) slab simulations consisting of 864 H_2O, 96 NaX, and 10 CH_3SO_3Na molecules. Panel (a): X = Cl; panel (b): X = SO_4. Small Z values correspond to slab interior.

Fig. 2 A snapshot from molecular dynamics (MD) simulation of a slab consisting of 864 H_2O, 96 Na_2SO_4, and 10 CH_3SO_3Na molecules. Color coding: Na-green, C-cyan, O-red, H—white, S in SO_4^{2-} ions—blue , H—white, S in $CH_3SO_3^-$ ions—yellow.

Table 3 Simulated changes in surface tension $\Delta\sigma$ of aqueous CH_3SO_3Na compared to pure water as a function of concentration. The mean statistical error of these values is ~ 1 dyne/cm
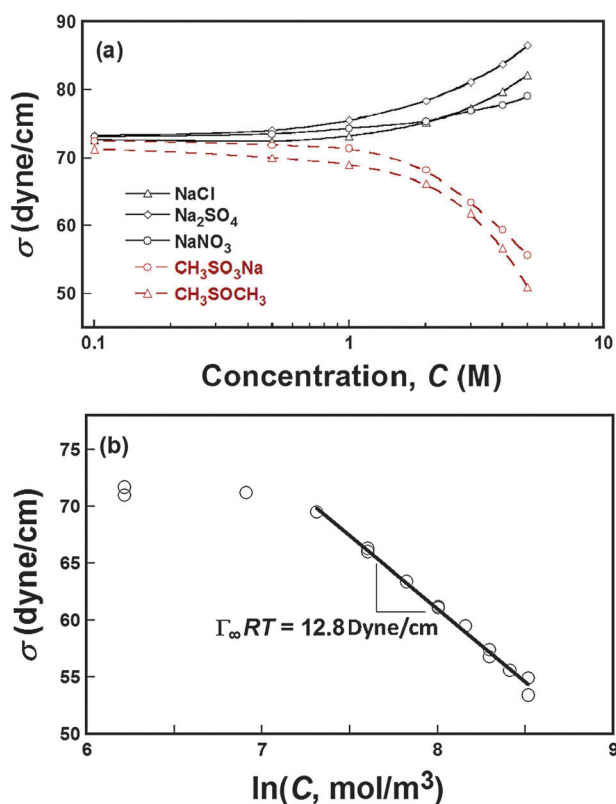
Molarity	$\Delta\sigma = \sigma - \sigma_{H_2O}$ (dyne/cm)
0.1	−0.6
0.5	−3.0
1.0	−8.6
1.5	−16.8
2.0	−21.9

solution/vapor interfaces are at the top and bottom of the image. A similar orientation of the hydrophobic methyl group was previously observed for the acetate ion.[61,62] The density profile indicates that chloride ion also exhibits a surface propensity,[63] although this propensity is much weaker than for $CH_3SO_3^-$. In contrast, both sodium and sulfate are repelled from the surface. These two ions have a strong tendency to pair and to aggregate in the subsurface area, which affects the water structure in the surface and subsurface.

Surface tension was extracted from the simulated anisotropy of the pressure tensor.[64] The results suggest a significant decrease of surface tension with an increased CH_3SO_3Na concentration (Table 3). Over the concentration range of 0.1 to 2 M, the variation of the surface tension computed is greater than experimental values, which will be reported below. The cause for the discrepancy is likely an overestimated ion pairing (particularly at the interface) due to inaccuracies in the force field.

Fig. 3 shows the experimental surface tension isotherms of aqueous solutions of NaCl, Na_2SO_4, $NaNO_3$, CH_3SO_3Na and CH_3OCH_3Na measured at room temperature. Based on the decay of the surface tension with increasing solute concentrations, a characteristic lyophobic behavior for both CH_3SO_3Na and CH_3OCH_3Na salts is observed. Therefore, CH_3SO_3Na tends

to concentrate on the droplet surface, in agreement with the MD results. From the surface tension measurements, the surface concentration of CH_3SO_3Na (Γ) may be estimated from the Gibbs isotherm for an ideal solution,

$$\left(\frac{\partial\sigma}{\partial\ln C}\right)_{p,T} \cong -\Gamma_\infty RT, \qquad (3)$$

where C is the molar concentration and R is the gas constant. For the CH_3SO_3Na solutions, the slope from a plot of σ versus $\ln C$ yields a $\Gamma_\infty RT$ value equal to 12.8 dyne/cm, as shown in Fig. 3b, where Γ_∞ denotes the surface concentration of $CH_3SO_3^-$ at the saturated limit of an aqueous CH_3SO_3Na solution. Based on the value of the slope, we calculated $\Gamma_\infty = 3 \times 10^{14}$ cm^{-2} at 298.2 K. This surface concentration corresponds to a surface area of 0.33 nm^2 per molecule. We should note here that in reality the surface concentration can be somewhat different due to non-ideal behavior.

Using the thermodynamic properties and hygroscopic growth data of NaCl particles,[65] at 75% RH, the growth factor of particle size is calculated to be 1.8, i.e., a 0.85 μm dry particle grows to 1.5 μm droplet when deliquesced. At this droplet size, if all CH_3SO_3Na molecules are in the surface layer, the minimum molar concentration of CH_3SO_3Na

11850 | *Phys. Chem. Chem. Phys.*, 2011, **13**, 11846–11857

This journal is © the Owner Societies 2011

Fig. 3 (a) Surface tension, σ, as a function of concentration (b) a surface tension isotherm of aqueous CH_3SO_3Na. Symbols are experimental data; lines in panel (a) are drawn to guide the eye; the line in panel (b) is a linear fit to data.

corresponding to saturated surface coverage is ~ 0.0175 M. Assuming a corresponding NaCl concentration of 6 M, a CH_3SO_3Na/NaCl ratio greater than ~ 0.0035 would be sufficient to cover the entire particle surface with $CH_3SO_3^-$ ions. This estimated ratio is well below the mixing ratios of $\sim 0.01-0.1$ characteristic, for instance, for the ambient sea salt particles present along the ocean shore in northern California.[30] Given the surfactant properties of CH_3SO_3Na and that it does not react with $HNO_3(g)$ (see Table 1), we expect that even small amounts of this salt may inhibit the heterogeneous reactivity of the entire CH_3SO_3Na/NaCl particle with HNO_3 (and possibly with other gas-phase species). At a given concentration, the degree to which the droplet surface can be covered by CH_3SO_3Na is droplet size dependent. However, even for particles as small as 0.1 μm the CH_3SO_3Na/NaCl ratio necessary to cover the particle surface with $CH_3SO_3^-$ is ~ 0.05, well within the range reported for ambient particles.

At lower RH, when mixed CH_3SO_3Na/NaCl particles begin to dehydrate, because of their different water solubility, NaCl crystallizes first and then CH_3SO_3Na crystallizes. The solubility of CH_3SO_3Na and NaCl salts in 100 cm³ of water at $T = 25$ °C are at least 90 g (determined in the course of this work) and 40 g,[66] respectively. Hence, dry CH_3SO_3Na/NaCl particles have a multilayered structure with the methanesulfonate salt concentrated on the top layer. This structure may change the hydration response and reactivity of the particles compared to those of pure NaCl. For effloresced, mixed CH_3SO_3Na/NaCl

particles with 0.01–0.1 mixing ratios and diameters of ~ 0.85 μm, the surface density of $CH_3SO_3^-$ should exceed 3×10^{14} cm^{-2}. Hence, the impact of CH_3SO_3Na on HNO_3 reactive uptake in mixed CH_3SO_3Na/NaCl particles at lower RH should be more significant, as we show in a subsequent section.

SEM/EDX mapping and TOF-SIMS depth profiling were used to interrogate the internal composition of dry CH_3SO_3Na/NaCl particles. Fig. 4 displays an SEM image and EDX elemental maps of two dry particles with mixing ratios of 0.05. As expected, no discernible spatial variations in Na and Cl were observed over the particles, but the intensities of S and O are clearly higher in the particle shell areas, which is indicative of $CH_3SO_3^-$ enrichment on the particle surface.

To further confirm the multilayer structure of dry CH_3SO_3Na/NaCl particles, TOF-SIMS depth profiling was performed on particles (mixing ratio = 0.1) collected on a silicon wafer. The top panel of Fig. 5 shows spatial distributions of the Cl^- and Na^+ ions recorded over two separate portions of the sample during negative and positive experimental modes, respectively. The maps indicate the location of particles probed in two experiments. Intensities of Cl^-, O^-, OH^-, SO_3^-, and Na^+ TOF-SIMS signals as a function of time (which corresponds to depth from the particle surface) are shown in the bottom panel of Fig. 5. As anticipated, the SO_3^-, O^-, and OH^- ion signals decrease rapidly at the beginning of the depth profiling, whereas the Na^+ and Cl^- ion signals both exhibit characteristic but somewhat different rise-and-fall behaviors. The Na^+ ion signal reaches a maximum intensity within the first 5 s, probably due to surface contamination. The Cl^- ion signal peaks near 80 s due to the CH_3SO_3Na surface coating, which is consistent with temporal profiles of SO_3^-, O^- and OH^- ions. The signal then levels off for about 500 s, and gradually drops afterwards. Based on a half-life of ~ 1800 s observed in these experiments for the decay of the Cl^- and Na^+ ion signals and the known ~ 1 μm size of particles, we estimate a depth profiling rate of 0.28 nm s^{-1} for these experimental conditions. Therefore, the CH_3SO_3Na surface layer is calculated to be ~ 25 nm thick. All of the ion-count profiles are consistent with the SEM findings, indicating a core-shell, multilayer structure in CH_3SO_3Na/NaCl particles: a NaCl core and a CH_3SO_3Na shell.

Hygroscopic behavior of mixed CH_3SO_3Na/NaCl particles

During hydration and dehydration, particles change their size, phase and water-to-solute ratios—physicochemical properties critical to the understanding of the heterogeneous reactive uptake. Fig. 6a shows the FTIR spectra recorded for mixed CH_3SO_3Na/NaCl particles with the mixing ratio of 0.1 during the hydration cycle at increased RH. The absorption band due to $\nu_8(-SO_3^-)$ asymmetric stretch is clearly observed at 1201 cm^{-1} over the entire range of RH. In the high RH spectra, the appearance of the $\nu(H_2O)$ stretching and the $\delta(H_2O)$ bending bands at ~ 3400 and ~ 1640 cm^{-1}, respectively, indicate the presence of condensed-phase water. The integrated absorbance of the $\nu(H_2O)$ band (from 3660 to 2750 cm^{-1}) was used to quantify the amount of water present in the particles.[51,52] Condensed-phase water is not detected until $\sim 69\%$ RH, at which point the $\nu(H_2O)$ and $\delta(H_2O)$
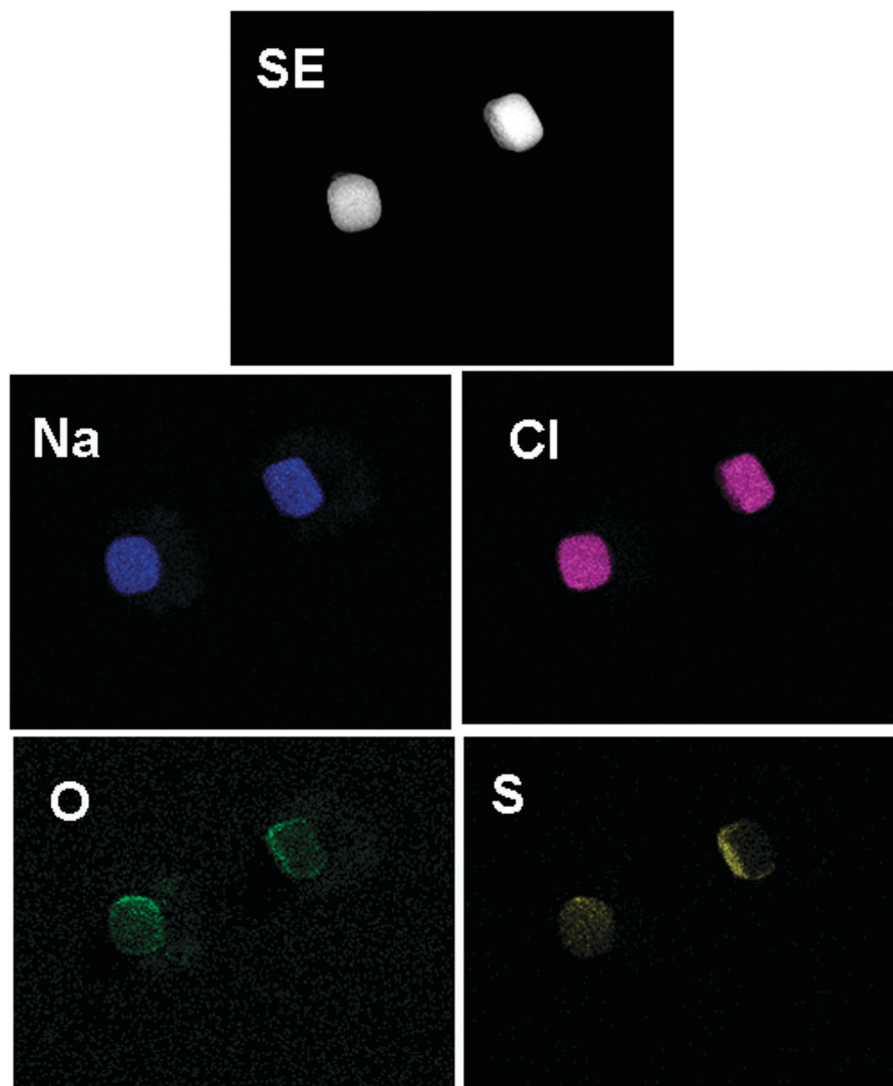
Fig. 4 Secondary electron image and X-ray elemental maps (Na, Cl, O and S) of $CH_3SO_3Na/NaCl$ particles with the mixing ratio of 0.05.

absorption bands begin to appear. At this RH, the CH_3SO_3Na shell becomes aqueous as indicated by a rapid increase in the absorbance of the water bands. Further increase in the RH to 75% shows a considerably greater amount of water taken up due to the dissolution of the NaCl core. At higher RH, completely aqueous droplets are formed and which continue to grow hygroscopically.

Fig. 6b combines the results of a hydration/dehydration experiment on $CH_3SO_3Na/NaCl$ particles. The change of water content is expressed as the $\nu(H_2O)$ band intensity at a specific RH (integrated from 3660 to 2750 cm^{-1}), normalized to that at 80% RH. The normalized values are plotted as a function of RH. For comparison, experimental data[52,65] for pure NaCl particles are also included. The phase transitions observed and the extent of the water uptake and dehydration agree well with the hygroscopic properties of pure CH_3SO_3Na and NaCl particles, for which reported deliquescence RH values are 71%[51] and 75%,[65] respectively. Above 69% RH, the water content of the $CH_3SO_3Na/NaCl$ particles initially increases due to the deliquescence of the CH_3SO_3Na component. The subsequent deliquescence of NaCl results in a second,

abrupt change in the water uptake at 75% RH. Upon evaporation, the particles slowly shed their water content until the RH reaches $\sim 47\%$ efflorescence relative humidity (ERH), where crystallization occurs. In contrast to the hydration behavior, no distinct two-step efflorescence event was observed in the dehydration experiment. This could arise from the close ERH values of pure CH_3SO_3Na and NaCl particles and lower accuracy of the efflorescence detection in experiments with substrate deposited particles.[52]

Heterogeneous uptake kinetics of HNO$_3$ on mixed CH$_3$SO$_3$Na/NaCl particles

Fig. 7 shows typical SEM images of $CH_3SO_3Na/NaCl$ particles before and after exposure to gas-phase HNO_3. Morphological changes indicative of reactive transformation are clearly seen. EDX spectra reveal a depletion of chlorine after the reaction. The experimental net uptake coefficient (γ_{net}) is calculated[49] from

$$\gamma_{net} = \frac{4k_I[Cl^-]_{d,0}}{\bar{c}_{HNO_3}[HNO_3]_\infty} \frac{V_d}{S_d} = \frac{2[Cl^-]_{d,0}\overline{D}_d}{3\bar{c}_{HNO_3}} \frac{k_I}{[HNO_3]_\infty} \quad (4)$$
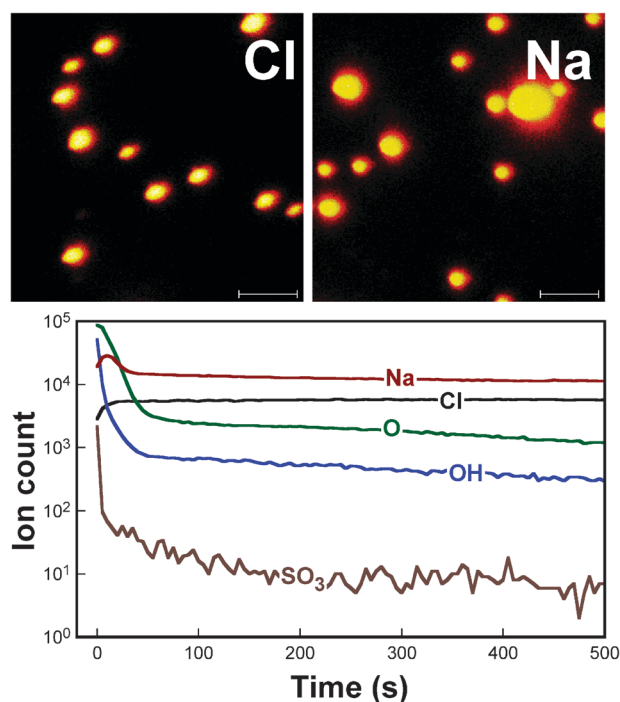
Fig. 5 TOF-SIMS analysis of CH₃SO₃Na/NaCl particles with the mixing ratio of 0.1. Top panel: maps of Cl⁻ and Na⁺ ions recorded over two separates areas of the sample. Size bar is 3 µm. Bottom panel: intensities of Cl⁻, O⁻, OH⁻, SO₃⁻, and Na⁺ ions as a function of time recorded in two depth profiling experiments (positive and negative modes).

where V_d/S_d is the droplet volume-to-surface area ratio, $\bar{c}_{HNO_3} = 3.18 \times 10^4$ cm s⁻¹ is the mean molecular speed of HNO₃, $\bar{D}_d$ is the deliquesced droplet or dry particle diameter, depending on the RH, and k_I is the pseudo-first-order rate constant in the limit of small particle loading ($N_s \rightarrow 0$) determined from EDX measurements and using eqn (2).[49,56] Eqn (4) would be exact if the heterogeneous reaction occured around the entire sphere of the droplet. However, the substrate-based experiment limits the gaseous reactant flux to a hemisphere rather than the entire droplet. To account for this, the uptake coefficient reported here is twice of that directly measured, i.e.,

$$\gamma_{net} = \frac{4[Cl^-]_{d,0}\bar{D}_d}{3\bar{c}_{HNO_3}} \frac{k_I}{[HNO_3]_\infty}, \qquad (5)$$

According to eqn (5), the particle size and initial concentration of chloride are required for uptake coefficient calculations. For experiments at RH = 40% (below the efflorescence point), the dry particle diameter (0.85 µm) was used. For experiments at 60 and 80% RH, the particle (droplet) diameters were estimated as 1.4 µm and 1.6 µm, respectively, using the hygroscopic growth data of NaCl particles[65] Literature[24] values for the RH-dependent chloride concentration in NaCl particles were used to estimate initial chloride concentrations in the mixed CH₃SO₃Na/NaCl particles. Namely, the following values of [Cl⁻]$_{d,0}$ were estimated: 37, 30, 11 and 6 M at 20, 40, 60 and 80% RH, respectively.
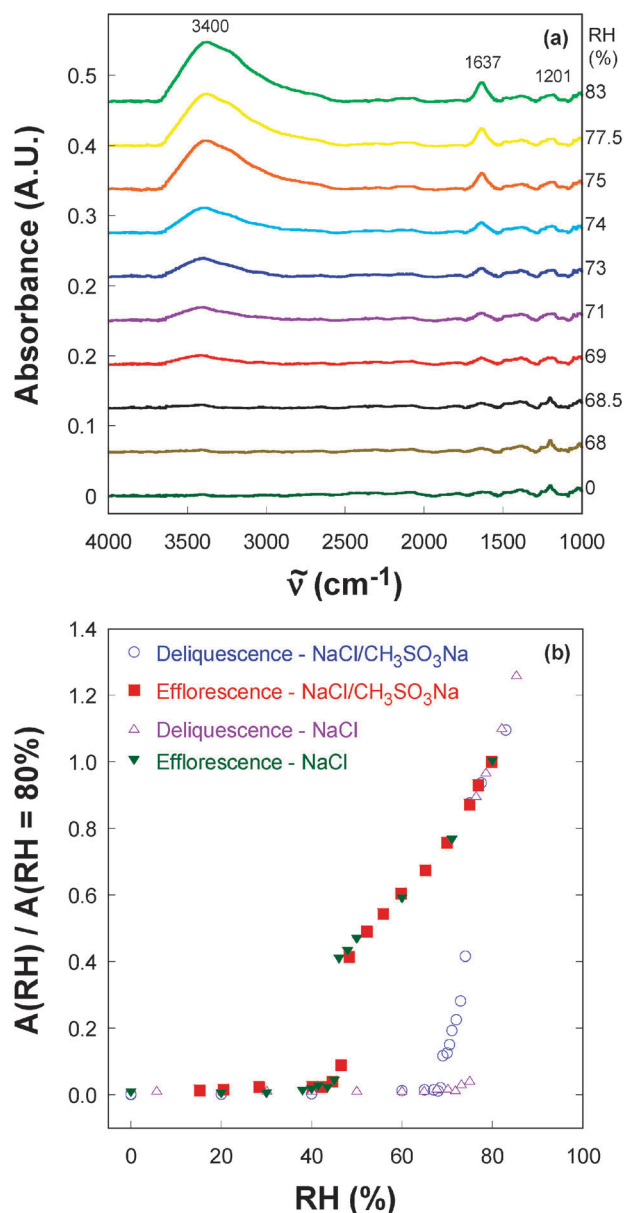

Fig. 6 (a) FTIR spectra of CH₃SO₃Na/NaCl particles (mixing ratio = 0.1) exposed to increasing% RH. (b) Representation of hydroscopic growth by ratios of integrated area of OH stretching mode relative to that at RH = 80%, measured for the same CH₃SO₃Na/NaCl particles in hydration and dehydration experiments. Data of NaCl is included for comparison (Liu et al., 2007).

A typical plot of γ_{net} values versus N_s is shown in Fig. 8. For comparison, the reactive uptake coefficients of HNO₃ on NaCl determined in a previous study[49] are also included in the figure. Trend lines in the plot represent nonlinear fits to data using the equation:[56] $\gamma_{net}(N_S) = (1/\gamma_{net(N_S \rightarrow 0)} + cN_S)^{-1}$. Corresponding values of γ_{net} in the limit of small particle loading ($N_s \rightarrow 0$) are summarized in Table 4. The uncertainty factors of the measured γ_{net} values were determined in the same manner as in the previous work.[49,50] For deliquesced particles at 80% RH, the reactive uptake of HNO₃ does not exhibit measurable differences with varying CH₃SO₃Na/NaCl
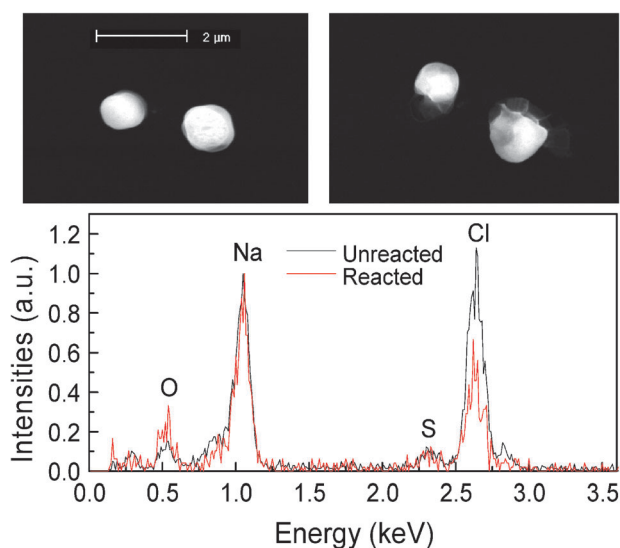
Fig. 7 Top panels: SEM images of $CH_3SO_3Na/NaCl$ particles before (left) and after (right) reaction with 11.6 ppb of gaseous HNO_3 at 80% RH for 15 min. Bottom panel: representative EDX spectra of an individual $CH_3SO_3Na/NaCl$ particle before and after reaction.
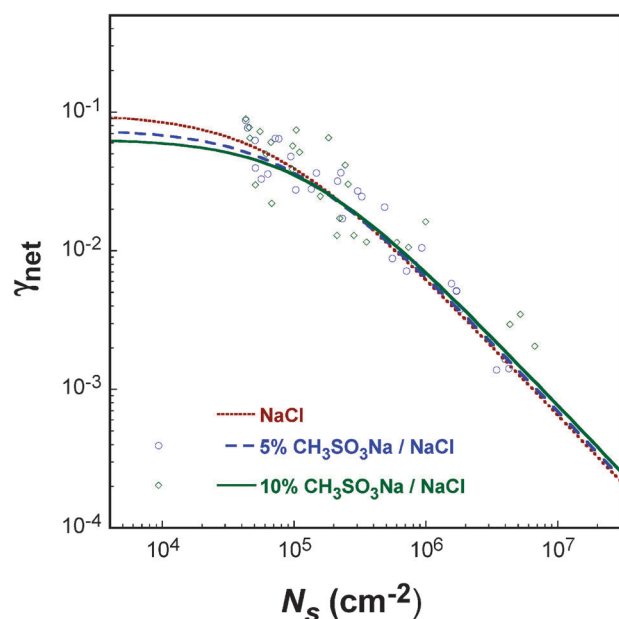
Fig. 8 γ_{net} values for $CH_3SO_3Na/NaCl$ particles with mixing ratios of 0.05 and 0.1 measured at RH = 80% as a function of particle number density N_s on the substrate surface. Symbols: experimental data, lines: fit to data. The curve fitted γ_{net} values for pure NaCl particles from Liu et al., 2007[49] are shown for comparison.

mixing ratios. The uptake coefficients γ_{net} are slightly lower than that measured for pure NaCl particles using the identical experimental procedure.[49] However, these differences are within the experimental uncertainty and therefore do not confirm that CH_3SO_3Na is inhibiting the reaction. Rather, the results indicate that the $CH_3SO_3^-$ accumulation on droplet surfaces does not alter substantially the heterogeneous reactivity of NaCl with gas-phase HNO_3. For typical sizes of sea salt

particles (a few micrometres), gas-phase diffusion of HNO_3 is the rate limiting step in the reactive uptake of HNO_3 onto NaCl. The $CH_3SO_3^-$ surfactant layer does not appear to affect the interfacial transport of HNO_3 strongly enough to become the rate determining step, i.e., transport across the gas-particle interface is still faster than the gas-phase diffusion.

Additional series of experiments were carried out at 20 and 40% RH, below the efflorescence point of mixed $CH_3SO_3Na/$ NaCl particles. The mixing ratios were varied (0.02, 0.05 and 0.1) to investigate how the amount of surface covered with CH_3SO_3Na affects HNO_3 uptake. The measured reactive uptake coefficients γ_{net} ($N_s \rightarrow 0$) are listed in Table 4. Unlike the data obtained at 80% RH, significant and consistent reduction of γ_{net} values was observed below the efflorescence RH. Under these conditions, the reactive uptake is limited by the chemical kinetics of HNO_3 reacting on the surface of NaCl crystals,[2] and not by the gas-phase diffusion. Heterogeneous reaction of HNO_3 with solid NaCl occurs at surface reactive sites-surface defects, steps and edges, and is limited by the availability of these sites. The inhibiting effect observed for mixed $CH_3SO_3Na/NaCl$ particles is associated with covering the reactive sites on the NaCl core by the non-reactive CH_3SO_3Na shell. The suppression of the reactive uptake for RH below efflorescence is consistently observed over the entire range of CH_3SO_3Na surface coverage. If we assume a spherical core-shell structure for the 0.85 μm particle and the cross section of the CH_3SO_3Na molecule of 18 Å^2, approximately 7 layers of CH_3SO_3Na cover the NaCl surface at a mixing ratio of 0.01. Therefore, it is not surprising that even at the lowest coverage, the γ_{net} value decreases by a factor of two. Additionally, the uptake coefficient decreases for particles with larger $CH_3SO_3Na/NaCl$ mixing ratios which would have higher surface coverage of CH_3SO_3Na. For the $CH_3SO_3Na/NaCl$ mixing ratio of 0.1, the reactive uptake is five times smaller than that of pure NaCl. However, some reaction still occurs, indicating that surface coverage of NaCl by CH_3SO_3Na is imperfect. This conclusion is also supported by the SEM/EDX mapping image shown in Fig. 4.

It is known that reactive uptake on dry NaCl particles is highly dependent on the amount of surface absorbed water[2] even though the particles are in a solid, crystalline phase. Measured uptake coefficients for $CH_3SO_3Na/NaCl$ particles with a mixing ratio of 0.1 (see Table 4) indicate persistent inhibition of reactive uptake on the mixed particles over the entire range of RH, as compared to pure NaCl particles. The inhibiting effect is around a factor of two for 60% RH, and the effect is more pronounced for 40% and 20% RH, where the uptake rate drops by a factor of 5. Again, this trend is consistent with a core-shell structure of mixed $CH_3SO_3Na/NaCl$ particles and with a CH_3SO_3Na shell that is inert towards reaction with HNO_3.

Although CH_3SO_3Na is expected to be unreactive towards HNO_3 (based on thermochemistry considerations) the lack of reaction was confirmed experimentally. We exposed pure CH_3SO_3Na particles to very high concentration of HNO_3 ($\sim$80 ppb) at 80% RH for over 10 h and analyzed the changes in the S/Na ratio. The CCSEM/EDX results showed no measurable differences before and after the exposure. If the uncertainty of the S/Na values was taken as an estimation of

Table 4 Experimental uptake coefficients (γ_{net}) for the heterogeneous reaction of HNO$_3$ with mixed CH$_3$SO$_3$Na/NaCl particles measured at different RH conditions. Data for NaCl particles are taken from Liu *et al.*, 2007

| Composition	80% RH D_d = 1.6 µm	60% RH D_d = 1.4 µm	40% RH D_d = 0.85 µm	20% RH D_d = 0.85 µm
NaCl	0.11 (×2.9/÷2.8)	0.20 (×2.9/÷2.8)	0.10 (×2.9/÷2.8)	0.02 (×2.9/÷2.8)
CH$_3$SO$_3$Na/NaCl (2/100)	—	—	0.05 (×2.9/÷2.8)	—
CH$_3$SO$_3$Na/NaCl (5/100)	0.09 (×2.5/÷2.5)	—	0.035 (×2.9/÷2.8)	—
CH$_3$SO$_3$Na/NaCl (10/100)	0.08 (×2.5/÷2.5)	0.09 (×2.5/÷2.5)	0.020 (×2.5/÷2.5)	0.003 (×2.5/÷2.5)
CH$_3$SO$_3$Na	< 10^{-5}	—	—	—

the possible reaction extent, an upper limit for γ_{net} of 10^{-5} for the uptake of HNO$_3$ onto CH$_3$SO$_3$Na particles is obtained.

Conclusions

In this study, surface activity of CH$_3$SO$_3^-$ ions in aqueous (deliquesced) particles, and shell–core structures of dry mixed CH$_3$SO$_3$Na/NaCl particles were investigated using a combination of experimental and modeling approaches for chemical imaging. The results suggest that surfaces of aqueous (deliquesced) sea salt particles contain substantial amount of CH$_3$SO$_3^-$ ions, while in the dry (effloresced) particles, methanesulfonate salts may form a layer of coating that modifies particle hygroscopicity and atmospheric reactivity. Water and HNO$_3$ reactive uptake measurements were carried out to assess the effects of particle internal composition on these properties. Consistent with the core-shell structures, the initial uptake of water by dry particles is governed by the hygroscopicity of the CH$_3$SO$_3$Na shell that deliquesces at 68–69% RH, followed by the NaCl deliquescence at 75–76% RH. However, addition of the CH$_3$SO$_3^-$ ions shows no detectable impact on the efflorescence RH. We have shown that the CH$_3$SO$_3$Na shell in dry particles inhibits their reactivity with HNO$_3$ and presumably also with nitrogen oxides. The inhibition is more substantial at lower RH, and higher CH$_3$SO$_3$Na concentrations.

Accumulation of CH$_3$SO$_3$Na salt on the surface of evaporating particles is a result of its higher solubility with respect to NaCl. However, in an atmospheric environment, dehydration behavior and internal composition of multi-component sea salt particles processed with CH$_3$SO$_3$H will be more complex because of highly soluble magnesium, potassium, and ammonium salts (MgSO$_4$·H$_2$O, KMgCl$_3$·6H$_2$O, NH$_3$HSO$_4$ *etc.*) that may also accumulate on the particle surface. Fig. 9 shows X-ray spectromicroscopy chemical maps of sulfur containing salts in individual marine particles collected in MASE 2005 field study.[30] Complex, non homogeneous distribution of CH$_3$SO$_3^-$ and SO$_4^{2-}$ salts in individual particles can be inferred from a range of CH$_3$SO$_3^-$/SO$_4^{2-}$ ratios measured for different particles areas as indicated by red and yellow colors. Qualitatively, the presence of both CH$_3$SO$_3^-$ and SO$_4^{2-}$ salts at particle edges is suggested from these maps. Surface accumulation of sulfates will have similar inhibiting impact on the atmospheric reactivity of dry sea salt particles, while chlorides present on the surface may have somewhat replenishing effects. The influence of other highly soluble salts and quantitative speciation of surface chemical composition of real sea salt particles are interesting topics for additional investigations following the case study presented here.
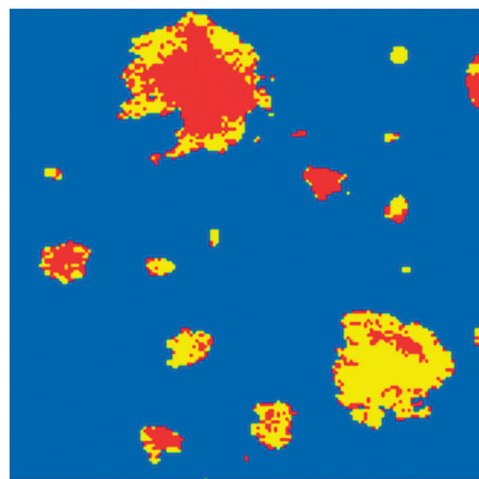
Fig. 9 STXM/NEXAFS chemical map (12 µm × 12 µm) of sulfur constituents in a sample of individual marine particles collected at the Point Reyes National Seashore, California, during MASE 2005 experiment. Two types of externally mixed particles have been reported in this sample: sea salt and sulfate particles. Red and yellow colors indicate portions of particles with CH$_3$SO$_3^-$/SO$_4^{2-}$ ratios above and below 20/80, respectively. Specific details of the STXM/NEXAFS analysis of these particles can be found in Hopkins *et al.*, 2007.

Appendix

Standard Gibbs free energy of selected aqueous salts (Table 5)

Gibbs free energy of formation of methylsulfonate acid and salts. The Gibbs free energy of formation for the CH$_3$SO$_3^-$ anion is estimated from the CH$_3$SO$_3$H acid dissociation constant. The pK_a value for CH$_3$SO$_3$H CH$_3$SO$_3^-$ + H$^+$ is −1.2.[68] Thus, ΔG_f°(CH$_3$SO$_3^-$)$_{ai}$ can be determined using the following equation:

$$\Delta G_r^\circ = -RT \ln K_a = 2.303 RT pK_a,$$

which yields the Gibbs free energy of reaction $\Delta G_r^\circ = -15.78$ kJ/mol. The standard Gibbs free energy of formation of CH$_3$SO$_3$H$_{(aq)}$ is −527.3 kJ/mol.[69] Hence, ΔG_f°(CH$_3$SO$_3^-$)$_{aq}$ is −543.1 kJ/mol. Unfortunately, the free energy $\Delta G_{r,S1}^\circ$ for

$$\text{CH}_3\text{SO}_3\text{Na}_{(aq)} \rightleftharpoons \text{CH}_3\text{SO}_3^-{}_{(aq)} + \text{Na}^+{}_{(aq)} \qquad (S1)$$
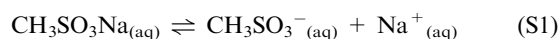
is not available, but its value is expected to be negative and typically a few kcal/mol. We find

$$\Delta G_f^\circ(\text{CH}_3\text{SO}_3\text{Na})_{ai} = \Delta G_f^\circ(\text{Na}^+)_{ai} + \Delta G_f^\circ(\text{CH}_3\text{SO}_3^-)_{ai}$$
$$- \Delta G_{r,S1}^\circ > -805.0 \text{ kJ/mol}. \qquad (1)$$

Table 5 Standard Gibbs free energy of formation of aqueous salts

Species	ΔG_f° (kJ/mol^{-1})	References
$NaCl_{(aq)}$	−393.1	Lide (2008)[66]
$Na_2SO_{4(aq)}$	−1268.4	Lide (2008)[66]
$NaHSO_{4(aq)}$	−1017.8	Lide (2008)[66]
$NaNO_{3(aq)}$	−373.2	Lide (2008)[66]
$(NH_4)SO_{4(aq)}$	−903.1	Lide (2008)[66]
$CH_3SO_3Na_{(aq)}$	> −805.0	Estimated, this work
$CH_3SO_3NH_{4(aq)}$	> −622.5	Estimated, this work
$H_2SO_{4(aq)}$	−744.5	Lide (2008)[66]
$CH_3SO_3H_{(aq)}$	−527.3	Guthrie and Gallant (2000)[67]
$HNO_{3(aq)}$	−111.3	Lide (2008)[66]
$HCl_{(aq)}$	−131.2	Lide (2008)[66]
$HCl_{(g)}$	−95.3	Lide (2008)[66]

where $\Delta G_f^\circ(Na^+)_{ai}$ is −261.9 kJ mol^{-1},[70] Likewise, since $\Delta G_f^\circ(NH_4^+)_{ai}$ is −79.4 kJ,[70] we find $\Delta G_f^\circ(CH_3SO_3NH_4)_{ai}$ to be > −622.5 kJ/mol.

Acknowledgements

References

1 W. C. Keene and D. L. Savoie, *Geophys. Res. Lett.*, 1998, **25**, 2181.
2 B. J. Finlayson-Pitts and J. C. Hemminger, *J. Phys. Chem. A*, 2000, **104**, 11463.
3 W. C. Keene, A. A. P. Pszenny, D. J. Jacob, R. A. Duce, J. N. Galloway, J. J. Schultz-Tokos, H. Sievering and J. F. Boatman, *Global Biogeochem. Cycles*, 1990, **4**, 407.
4 A. A. P. Pszenny, W. C. Keene, D. J. Jacob, S. Fan, J. R. Maben, M. P. Zetwo, M. Springer-Young and J. N. Galloway, *Geophys. Res. Lett.*, 1993, **20**, 699.
5 G. P. Ayers, R. W. Gillett, J. M. Cainey and A. L. Dick, *J. Atmos. Chem.*, 1999, **33**, 299.
6 R. Gabriel, R. von Glasow, R. Sander, M. O. Andreae and P. J. Crutzen, *J. Geophys. Res.*, 2002, **107**, 8032.
7 K. Hara, K. Osada, M. Kido, M. Hayashi, K. Matsunaga, Y. Iwasaka, T. Yamanouchi, G. Hashida and T. Fukatsu, *J. Geophys. Res.*, 2004, **109**, D20208.
8 K. Hara, Y. Iwasaka, M. Wada, T. Ihara, H. Shiba, K. Osada and T. Yamanouchi, *J. Geophys. Res.*, 2006, **111**, D15216.
9 K. Hara, K. Osada, M. Kido, K. Matsunaga, Y. Iwasaka, G. Hashida and T. Yamanouchi, *Tellus, Ser. B*, 2005, **57**, 230.
10 R. C. Hoffman, M. E. Gebel, B. S. Fox and B. J. Finlayson-Pitts, *Phys. Chem. Chem. Phys.*, 2003, **5**, 1780.
11 J. M. Laux, T. F. Fister, B. J. Finlayson-Pitts and J. C. Hemminger, *J. Phys. Chem.*, 1996, **100**, 19891.
12 B. J. Finlayson-Pitts, *Chem. Rev.*, 2003, **103**, 4801.
13 J. A. Davies and R. A. Cox, *J. Phys. Chem. A*, 1998, **102**, 7631.
14 D. Sporleder and G. E. Ewing, *J. Phys. Chem. A*, 2001, **105**, 1838.
15 M.-T. Leu, R. S. Timonen, L. F. Keyser and Y. L. Yung, *J. Phys. Chem.*, 1995, **99**, 13203.
16 H. M. ten Brink, *J. Aerosol Sci.*, 1998, **29**, 57.
17 P. Beichert and B. J. Finlayson-Pitts, *J. Phys. Chem.*, 1996, **100**, 15218.
18 S. Ghosal and J. C. Hemminger, *J. Phys. Chem. A*, 1999, **103**, 4777.
19 S. J. Peters and G. E. Ewing, *J. Phys. Chem. B*, 1997, **101**, 10880.
20 S. J. Peters and G. E. Ewing, *Langmuir*, 1997, **13**, 6345.
21 H. C. Allen, J. M. Laux, R. Vogt, B. J. Finlayson-Pitts and J. C. Hemminger, *J. Phys. Chem.*, 1996, **100**, 6371.
22 J. P. D. Abbatt and G. C. G. Waschewsky, *J. Phys. Chem. A*, 1998, **102**, 3719.
23 M. P. Tolocka, T. D. Saul and M. V. Johnston, *J. Phys. Chem. A*, 2004, **108**, 2659.
24 T. D. Saul, M. P. Tolocka and M. V. Johnston, *J. Phys. Chem. A*, 2006, **110**, 7614.
25 M. C. Evans, S. W. Campbell, V. Bhethanabotla and N. D. Poor, *Atmos. Environ.*, 2004, **38**, 4847.
26 J. H. Seinfeld and S. N. Pandis, *Atmospheric Chemistry and Physics From Air Polution to Climate Change*, Wiley and Sons, Inc, New York, 2nd edn, 2006.
27 D. D. Lucas and R. G. Prinn, *J. Geophys. Res.*, 2002, **107**, 4201.
28 R. von Glasow and P. J. Crutzen, *Atmos. Chem. Phys.*, 2004, **4**, 589.
29 A. Laskin, D. J. Gaspar, W. Wang, S. W. Hunt, J. P. Cowin, S. D. Colson and B. J. Finlayson-Pitts, *Science*, 2003, **301**, 340.
30 R. J. Hopkins, Y. Desyaterik, A. V. Tivanski, R. A. Zaveri, C. M. Berkowitz, T. Tyliszczak, M. K. Gilles and A. Laskin, *Journal of Geophysical Research—Atmospheres*, 2007, **113**, D040209.
31 M. Posfai and P. R. Buseck, in *Annual Review of Earth and Planetary Sciences*, 2010, vol. 38, p. 17.
32 T. A. Semeniuk, M. E. Wise, S. T. Martin, L. M. Russell and P. R. Buseck, *Atmos. Environ.*, 2007, **41**, 6225.
33 M. E. Wise, E. J. Freney, C. A. Tyree, J. O. Allen, S. T. Martin, L. M. Russell and P. R. Buseck, *Journal of Geophysical Research-Atmospheres*, 2009, **114**.
34 M. E. Wise, T. A. Semeniuk, R. Bruintjes, S. T. Martin, L. M. Russell and P. R. Buseck, *Journal of Geophysical Research-Atmospheres*, 2007, **112**, Art. No. D10224.
35 X. K. Chen, B. Minofar, P. Jungwirth and H. C. Allen, *J. Phys. Chem. B*, 2010, **114**, 15546.
36 C. E. L. Myhre, B. D'Anna, F. M. Nicolaisen and C. J. Nielsen, *Appl. Opt.*, 2004, **43**, 2500.
37 I. Benjamin, *J. Chem. Phys.*, 1991, **95**, 3698.
38 M. A. Wilson and A. Pohorille, *J. Chem. Phys.*, 1991, **95**, 6005.
39 U. Essmann, L. Perera, M. L. Berkowitz, T. Darden, H. Lee and L. G. Pedersen, *J. Chem. Phys.*, 1995, **103**, 8577.
40 J.-P. Ryckaert, G. Ciccotti and H. J. C. Berendsen, *J. Comput. Phys.*, 1977, **23**, 327.
41 J. W. Caldwell and P. A. Kollman, *J. Phys. Chem.*, 1995, **99**, 6208.
42 J. Wang, R. M. Wolf, J. W. Caldwell, P. A. Kollman and D. A. Case, *J. Comput. Chem.*, 2004, **25**, 1157.
43 S. Gopalakrishnan, P. Jungwirth, D. J. Tobias and H. C. Allen, *J. Phys. Chem. B*, 2005, **109**, 8861.
44 M. J. Frisch, G. W. Trucks, H. B. Schlegel, G. E. Scuseria, M. A. Robb, J. R. Cheeseman, J. A. Montgomery, Jr., T. Vreven, K. N. Kudin, J. C. Burant, J. M. Millam, S. S. Iyengar, J. Tomasi, V. Barone, B. Mennucci, M. Cossi, G. Scalmani, N. Rega, G. A. Petersson, H. Nakatsuji, M. Hada, M. Ehara, K. Toyota, R. Fukuda, J. Hasegawa, M. Ishida,

T. Nakajima, Y. Honda, O. Kitao, H. Nakai, M. Klene, X. Li, J. E. Knox, H. P. Hratchian, J. B. Cross, V. Bakken, C. Adamo, J. Jaramillo, R. Gomperts, R. E. Stratmann, O. Yazyev, A. J. Austin, R. Cammi, C. Pomelli, J. W. Ochterski, P. Y. Ayala, K. Morokuma, G. A. Voth, P. Salvador, J. J. Dannenberg, V. G. Zakrzewski, S. Dapprich, A. D. Daniels, M. C. Strain, O. Farkas, D. K. Malick, A. D. Rabuck, K. Raghavachari, J. B. Foresman, J. V. Ortiz, Q. Cui, A. G. Baboul, S. Clifford, J. Cioslowski, B. B. Stefanov, G. Liu, A. Liashenko, P. Piskorz, I. Komaromi, R. L. Martin, D. J. Fox, T. Keith, M. A. Al-Laham, C. Y. Peng, A. Nanayakkara, M. Challacombe, P. M. W. Gill, B. Johnson, W. Chen, M. W. Wong, C. Gonzalez and J. A. Pople, C.02 edn, Gaussian, Inc, Wallingford, CT, 2004.

45 D. A. Case, T. A. Darden, T. E. Cheatham, III, C. L. Simmerling, J. Wang, R. E. Duke, R. Luo, R. C. Walker, W. Zhang, K. M. Merz, B. P. Roberts, B. Wang, S. Hayik, A. Roitberg, G. Seabra, I. Kolossváry, K. F. Wong, F. Paesani, J. Vanicek, J. Liu, X. Wu, S. R. Brozell, T. Steinbrecher, H. Gohlke, Q. Cai, X. Ye, J. Wang, M.-J. Hsieh, G. Cui, D. R. Roe, D. H. Mathews, M. G. Seetin, C. Sagui, V. Babin, T. Luchko, S. Gusarov, A. Kovalenko and P. A. Kollman, University of California—San Francisco, San Francisco, 2008.

46 *Handbook of Applied Surface and Colloid Chemistry*, ed. K. Holmberg, Wiley and Sons, New York, 2002, p. 219.

47 R. E. Johnson and R. H. Dettre, in *Surface and Colloid Science*, ed. E. Matijevic and F. R. Eirich, Academic Press, New York, 1969, vol. 2, p. 85.

48 A. W. Neumann and R. J. Good, in *Surface and Colloid Science*, ed. R. J. Good and R. R. Stromberg, Plenum Press, New York, 1979, vol. 11, p. 31.

49 Y. Liu, J. P. Cain, H. Wang and A. Laskin, *J. Phys. Chem. A*, 2007, **111**, 10026.

50 Y. Liu, E. R. Gibson, J. P. Cain, H. Wang, V. H. Grassian and A. Laskin, *J. Phys. Chem. A*, 2008, **112**, 1561.

51 Y. Liu and A. Laskin, *J. Phys. Chem. A*, 2009, **113**, 1531.

52 Y. Liu, Z. Yang, Y. Desyaterik, P. L. Gassman, H. Wang and A. Laskin, *Anal. Chem.*, 2008, **80**, 633.

53 Y. N. Hua, *J. Trace Microprobe Tech.*, 2003, **21**, 25.

54 A. Laskin, J. P. Cowin and M. J. Iedema, *J. Electron Spectrosc. Relat. Phenom.*, 2006, **150**, 260.

55 D. J. Gaspar, A. Laskin, W. Wang, S. W. Hunt and B. J. Finlayson-Pitts, *Appl. Surf. Sci.*, 2004, **231–232**, 520.

56 A. Laskin, H. Wang, W. H. Robertson, J. P. Cowin, M. J. Ezell and B. J. Finlayson-Pitts, *J. Phys. Chem. A*, 2006, **110**, 10619.

57 Y. Liu, J. P. Cain, H. Wang and A. Laskin, *J. Phys. Chem. A*, 2007, **111**, 10026.

58 S. V. Hering, D. R. Lawson, I. Allegrini, A. Febo, C. Perrino, M. Possanzini, J. E. Sickles, K. G. Anlauf, A. Wiebe, B. R. Appel, W. John, J. Ondo, S. Wall, R. S. Braman, R. Sutton, G. R. Cass, P. A. Solomon, D. J. Eatough, N. L. Eatough, E. C. Ellis, D. Grosjean, B. B. Hicks, J. D. Womack, J. Horrocks, K. T. Knapp, T. G. Ellestad, R. J. Paur, W. J. Mitchell, M. Pleasant, E. Peake, A. Maclean, W. R. Pierson, W. Brachaczek, H. I. Schiff, G. I. Mackay, C. W. Spicer, D. H. Stedman, A. M. Winer, H. W. Biermann and E. C. Tuazon, *Atmos. Environ.*, 1988, **22**, 1519.

59 Y. Liu, Z. W. Yang, Y. Desyaterik, P. L. Gassman, H. Wang and A. Laskin, *Anal. Chem.*, 2008, **80**, 7179.

60 I. N. Tang, A. C. Tridico and K. H. Fung, *J. Geophys. Res.*, 1997, **102**, 23269.

61 B. Minofar, P. Jungwirth, M. R. Das, W. Kunz and S. Mahiuddin, *J. Phys. Chem. C*, 2007, **111**, 8242.

62 B. Minofar, R. Vácha, A. Wahab, S. Mahiuddin, W. Kunz and P. Jungwirth, *J. Phys. Chem. B*, 2006, **110**, 15939.

63 L. Vrbka, M. Mucha, B. Minofar, P. Jungwirth, E. C. Brown and D. J. Tobias, *Curr. Opin. Colloid Interface Sci.*, 2004, **9**, 67.

64 Y. Zhang, S. E. Feller, B. R. Brooks and R. W. Pastor, *J. Chem. Phys.*, 1995, **103**, 10252.

65 I. N. Tang, *J. Geophys. Res.*, 1997, **102**, 1883.

66 *CRC Handbook of Chemistry and Physics*, ed. D. R. Lide, CRC Press, Boca Raton, FL, 88th edn, 2008.

67 J. P. Guthrie and R. T. Gallant, *Canadian Journal of Chemistry*, 2000, **78**, 1295.

68 A. Albert and E. P. Serjeant, *The Determination of Ionization Constants*, Chapman and Hall, New York, 1984.

69 J. P. Guthrie and R. T. Gallant, *Can. J. Chem.*, 2000, **78**, 1295.

70 *Codata Key Values for Thermodynamics*, ed. J. D. Cox, D. D. Wagman and V. A. Medvedev, Hemisphere Publishing Corp, New York, 1989.

This journal is © the Owner Societies 2011

Phys. Chem. Chem. Phys., 2011, **13**, 11846–11857 | 11857